ACS APPLIED MATERIALS & INTERFACES

www.acsami.org

Research Article

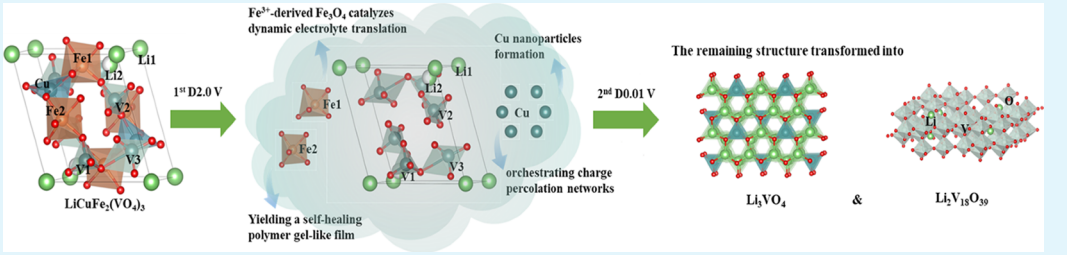
Self-Reinforcing Structural–Interfacial Evolution in $LiCuFe_2(VO_4)_3$ Anodes Enables Durable, High-Capacity Lithium Storage

Lihua Chu,‡ Haiyang Ye,‡ Shiqi Liu,‡ Junxiang Zhang, Jianan Gu, Mengwei Wang, Shangzhe Guo, Mengqing Li, Yuxin Shi, Xin Xia, Lehao Liu, Haifang Li, Bing Jiang, Christopher S. Blackman, and Meicheng Li*

Cite This: https://doi.org/10.1021/acsami.6c03927

Read Online

ACCESS | Metrics & More | Article Recommendations | Supporting Information



ABSTRACT: Designing high-capacity and durable anodes for lithium-ion batteries (LIBs) remains a formidable challenge due to persistent structural degradation and sluggish interfacial kinetics. Herein, a polycationic vanadate-based compound, $LiCuFe_2(VO_4)_3$, is engineered to address these issues through a coupled mechanism of electrochemical lattice reorganization and self-adaptive interface modulation. The electrode exhibits an exceptional cycling performance, retaining a specific capacity of 1178 mAh g^{-1} after 1000 cycles at 0.5 A g^{-1}, accompanied by a continuous capacity elevation phenomenon. Advanced synchrotron radiation X-ray diffraction and first-principles calculations reveal that, during cycling, the precipitation of metallic Cu nanoparticles orchestrates charge percolation networks, while Fe^{3+}-derived Fe_3O_4 catalyzes dynamic electrolyte translation, yielding a polymer gel-like film. This dual-regulation framework simultaneously alleviates mechanical stress and enables high-rate surface-dominated storage. These findings shed light on an electrochemically induced optimization paradigm, positioning $LiCuFe_2(VO_4)_3$ as a prototype material for next-generation high-performance LIB anode.

KEYWORDS: *vanadate anode, $LiCuFe_2(VO_4)_3$, conversion–intercalation hybrid lithium storage, electrochemical performance, lithium-ion batteries*

INTRODUCTION

The global deployment of battery-powered electronic devices necessitates the development of next-generation rechargeable batteries with enhanced energy density, cycling, and electrochemical stability. The commercial graphite anode, characterized by a low lithiation potential of ∼0.1 V and a modest theoretical capacity of 372 mAh g^{-1}, is insufficient to meet the stringent energy density and safety requirements of advanced electric vehicle systems.[1] To transcend the intrinsic capacity limitation of graphite, considerable research efforts have been devoted to the exploration of high-capacity anodes, including silicon-based materials (silicon theoretical capacity ∼4200 mAh g^{-1}; SiO_x, $0 < x < 2$, theoretical capacity ∼2600 mAh g^{-1}),[2,3] transition metal oxides such as SnO_2,[4,5] and transition metal sulfides/phosphides.[6] Although these candidates deliver remarkable theoretical capacities, their practical viability is fundamentally constrained by inherent challenges, including drastic volumetric expansion, mechanical pulverization with loss of active-material integrity, and interfacial instability that aggravates parasitic reactions, ultimately resulting in rapid capacity fading over prolonged cycling.

Transition metal vanadates have emerged as a compelling class of anode materials owing to their multielectron redox activity and structural stability.[7] Among them, Li_3VO_4 has been extensively investigated as one of the most promising anode candidates for LIBs, offering a relatively safe lithiation-potential window (1.0–0.5 V vs Li^+/Li) and a higher theoretical capacity (592 mAh g^{-1}) compared with graphite.[8] Nevertheless, its intrinsically poor electronic conductivity (<10^{-10} S m^{-1}) severely

Received: February 25, 2026
Revised: June 23, 2026
Accepted: July 7, 2026

ACS Publications © XXXX American Chemical Society

restricts charge transport and electrochemical kinetics, while interfacial instability and structural degradation lead to rapid capacity fading upon extended cycling.[9,10] Consequently, recent research has focused on enhancing not only electronic conductivity but also interfacial robustness to unlock the full electrochemical potential of Li_3VO_4. A particularly effective strategy involves the heteroatomic incorporation of transition metals (e.g., Fe, Cu) into the vanadate lattice, thereby modulating its electrochemical behavior, improving conductivity, and accelerating redox kinetics. Furthermore, emerging studies have shown that rational structural engineering can induce the *in situ* formation of metallic nanoparticles during cycling, enhancing electrode conductivity and alleviating kinetic limitations and interfacial polarization.[9,11] Concurrently, adaptive interfacial phenomena such as the electrochemically driven evolution of polymer gel-like films at the electrode–electrolyte interface can provide additional pseudocapacitive contributions and mechanical buffering, thereby extending electrode longevity.[12]

Building upon these insights, we rationally designed and synthesized a polycationic vanadate, $LiCuFe_2(VO_4)_3$, and comprehensively investigated its electrochemical behavior and underlying mechanism as an anode for LIBs. The electrode demonstrates exceptional cycling stability, operating at a safe lithiation potential of 0.4 V vs Li^+/Li and delivering a high reversible capacity of 1178 mAh g^{-1} after 1000 cycles at 0.5 A g^{-1}. First-principles calculations reveal that Li^+ preferentially interacts with adjacent sites of FeO_6 octahedra, where Fe^{3+} serves as the dominant redox center during lithiation. During cycling, the *in situ* precipitation of metallic Cu nanoparticles constructs conductive percolation networks, markedly enhancing the electronic conductivity of the electrode. Concurrently, the conversion of Fe^{3+} into Fe_3O_4 catalyzes dynamic electrolyte transformation, giving rise to a reversible polymer gel-like interfacial film that contributes interfacial charge storage via pseudocapacitive processes and mitigates mechanical stress. In parallel, the residual framework undergoes sequential phase transitions into Li_3VO_4 and $Li_2V_{18}O_{39}$, which accommodate Li^+ through a reversible insertion/extraction mechanism (Scheme 1). Collectively, these coupled structural and interfacial transformations account for the exceptional electrochemical stability and capacity retention of $LiCuFe_2(VO_4)_3$.

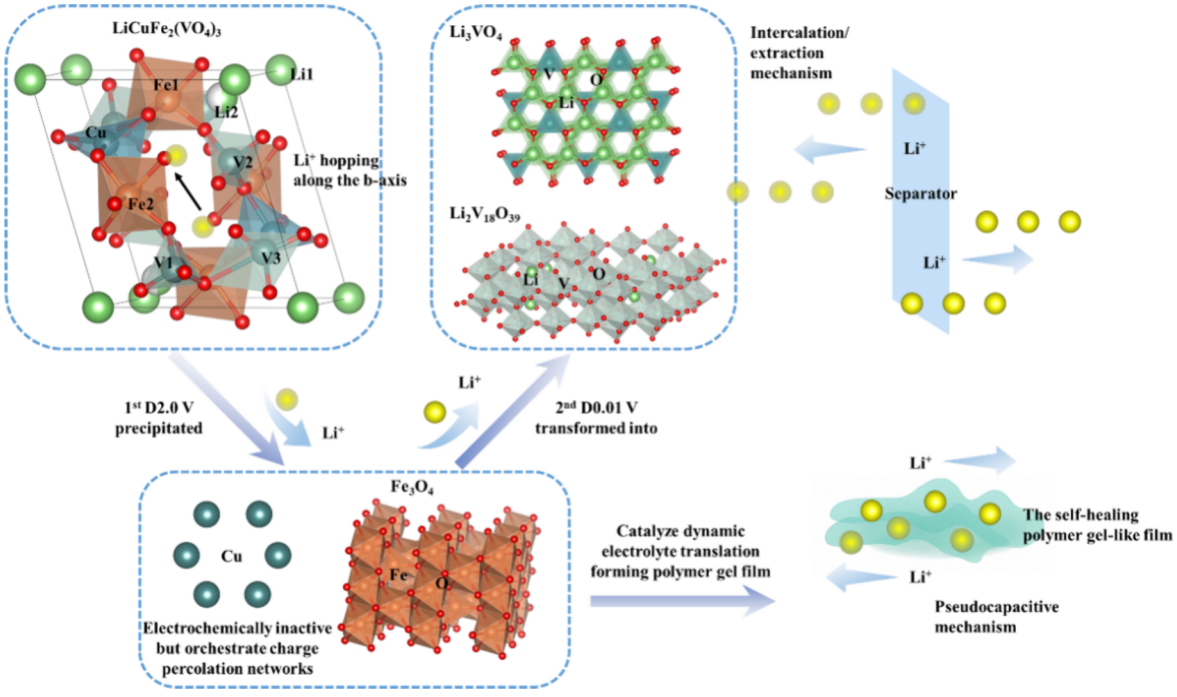
This study elucidates a self-reinforcing structure–interface evolution mechanism in $LiCuFe_2(VO_4)_3$ in which coupled lattice reorganization and interfacial adaptation jointly drive electrochemically induced self-optimization. Such a mechanism transforms the conventional degradation pathway of conversion-type electrodes into a self-stabilizing process, thereby achieving a synergistic enhancement in both capacity retention and cycling durability. Importantly, this work advances the understanding of structure–interface coupling in a multicomponent vanadate, offering mechanistic guidance for designing durable, high-capacity anodes for next-generation lithium-ion batteries.

RESULTS AND DISCUSSION

Characterization of $LiCuFe_2(VO_4)_3$

Rietveld refinement of the XRD pattern (Figure 1a) confirms the phase purity of $LiCuFe_2(VO_4)_3$, with diffraction peaks matching the reference (JCPDS no. 50-0212). The refinement residuals (R_{wp} = 2.77%, R_p = 1.88%, χ^2 = 1.75) indicate its high structural reliability. The refinement parameters (atomic position, atomic occupy, and temperature factor) are summarized in Table S1. The crystal structure of $LiCuFe_2(VO_4)_3$, refined through Rietveld analysis (Figure 1a and Figure S1), reveals a three-dimensional (3D) framework constructed via polyhedral connectivity. Two $Fe(1)O_6$ octahedra can share edges to form a dimer, and the $Fe(2)O_6$ dimer is formed similarly, while the two dimers are connected by co-edging with the

Scheme 1. Schematic Diagram of the Lithium Storage Mechanism of the $LiCuFe_2(VO_4)_3$ Anode



https://doi.org/10.1021/acsami.6c03927
ACS Appl. Mater. Interfaces XXXX, XXX, XXX–XXX

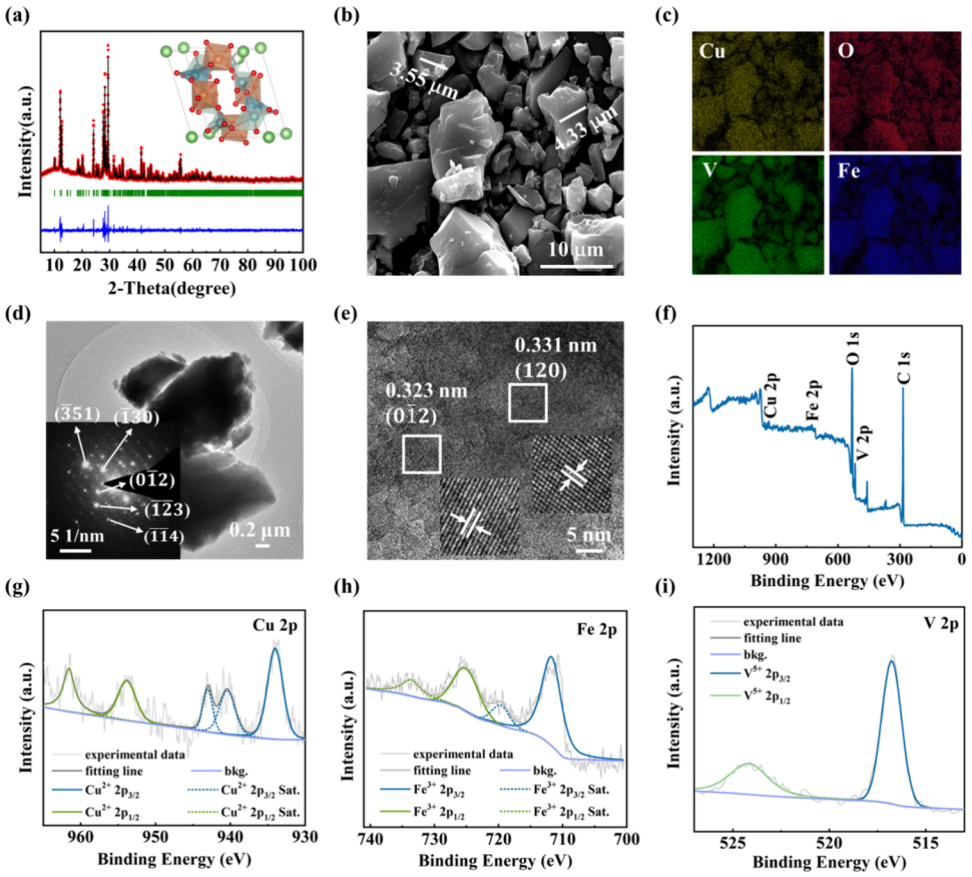


Figure 1. (a) XRD pattern at room temperature for $LiCuFe_2(VO_4)_3$. The red dots stand for the observed intensities; the black solid lines are the calculated profiles; green vertical lines show reflection positions. Differences between the observed and the calculated intensities are shown at the bottom of the figure. The inset shows the crystal structure for $LiCuFe_2(VO_4)_3$. (b) SEM image. (c) Surface element distribution image. (d) TEM image (inset is SAED). (e) HRTEM image of $LiCuFe_2(VO_4)_3$. (f) XPS survey spectrum of the as-prepared $LiCuFe_2(VO_4)_3$. (g–i) The corresponding high-resolution XPS spectra of Cu 2p (g), Fe 2p (h), and V 2p (i) peaks.

CuO_5 triangular bipyramid so that the Fe1-Fe1-Cu-Fe2-Fe2 twisted chains formed are interconnected with the surrounding VO_4 tetrahedra to create a 3D framework. This structure is occupied with lithium ions at two distinctly different sites, one of which is semi-occupied. During lithiation, the semi-occupied site is preferentially filled, and upon its saturation, further insertion triggers a structural transformation.[13,14]

The morphology and microstructure of the as-prepared $LiCuFe_2(VO_4)_3$ compound were elucidated via scanning electron microscopy (SEM) and transmission electron microscopy (TEM). As depicted in Figure 1b, the material exhibits an irregular, bulk-like morphology with a nonuniform particle size distribution. Furthermore, corresponding energy-dispersive X-ray spectroscopy (EDS) elemental mapping (Figure 1c) confirms that the constituent elements including V, O, Fe, and Cu are homogeneously distributed throughout the entire $LiCuFe_2(VO_4)_3$ matrix, verifying the compositional uniformity of the synthesized phase. As shown in Figure 1d, the prepared $LiCuFe_2(VO_4)_3$ exhibits stacked blocks. The inset shows the selected-area electron diffraction (SAED) results with clear and bright diffraction points, indicating that the sample is well crystallized and the calibrated crystal plane is consistent with the XRD results. High-resolution TEM (HRTEM, Figure 1e) resolves lattice fringes with interplanar spacings of 0.331 and 0.323 nm, corresponding to the crystal planes of (120) and $(0\bar{1}2)$ of $LiCuFe_2(VO_4)_3$, respectively, further validating the structural assignment.

Surface chemical states of the $LiCuFe_2(VO_4)_3$ were probed by X-ray photoelectron spectroscopy (XPS, Figure 1f–i). From the wide-scan survey spectrum (Figure 1f), the characteristic peaks of Cu 2p, Fe 2p, V 2p, and O 1s can be identified. At high resolution, the respective XPS spectra of Cu 2p, Fe 2p, and V 2p were further deconvoluted using the Gaussian method. The two peaks at 934.0 and 953.7 eV in Figure 1g correspond to Cu $2p_{3/2}$ and $2p_{1/2}$, confirming the presence of Cu^{2+}.[15] In addition, the binding energy peaks located at 940.4, 943.1, and 961.3 eV belong to its satellite peaks. The Fe 2p spectrum is typically located at 711.7 eV (Fe $2p_{3/2}$) and 725.1 eV (Fe $2p_{1/2}$), accompanied by two shakeup satellite peaks at 719.7 and 733.6 eV, characteristic of Fe^{3+} (Figure 1h).[16] The V 2p spectrum, as shown in Figure 1i, displays peaks with binding energies of 516.8 eV (V $2p_{3/2}$) and 524.2 eV (V $2p_{1/2}$), indicative of V^{5+}.[17,18]

Electrochemical Properties of the $LiCuFe_2(VO_4)_3$ Anode

To investigate the redox reactions of $LiCuFe_2(VO_4)_3$ during charge and discharge, cyclic voltammetry (CV) was conducted at a scanning rate of 0.1 mV s^{-1} over a voltage range of 0.01–3.00 V (vs Li/Li^+) (Figure 2a). In the initial discharge cycle, six main reduction peaks are observed. A prominent peak centered at 2.69 V is attributed to the preferential filling of the

https://doi.org/10.1021/acsami.6c03927
ACS Appl. Mater. Interfaces XXXX, XXX, XXX–XXX

semi-occupied site of Li^+ in the $LiCuFe_2(VO_4)_3$ lattice, yielding the phase of $Li_{1+x}CuFe_2(VO_4)_3$. This is followed by a reduction peak at 2.40 V, marking a lithiation-induced structural reorganization wherein additional Li^+ triggers a phase transition. The broad peak around 2.22 V is related to the conversion of Cu^{2+} to Cu^0 and the simultaneous generation of Fe_3O_4. Notably, the oxidation peak of Cu^0 to Cu^{2+} typically around 2.6 V in charging curves is absent in the initial charging CV curve of the $LiCuFe_2(VO_4)_3$ electrode.[19,20] This absence suggests that the formation of metallic Cu during the initial discharge is irreversible and does not participate in the subsequent electrochemical cycles.[21] Further Li^+ insertion into the electrode material causes a peak around 1.82 V.[22] The peak located at 0.65 V is attributed to further changes in the valence state of Fe.[23] The peaks at 2.69, 2.40, 2.22, and 1.82 V either disappeared or shifted slightly in subsequent cycles, indicating a partial irreversible reaction during the first cycle discharge. The broad peak at 0.25 V is due to valence state changes of V and the irreversible formation of the solid electrolyte interface phase (SEI) from the reaction between the material and electrolyte.[24] During charging, two main oxidation peaks are observed: the peak at 1.34 V is assigned to the valence state changes of V, while the peak at 1.93 V signifies the valence state changes of Fe. The first CV curve of $LiCuFe_2(VO_4)_3$ exhibits distinct discharge and charge behaviors compared to the subsequent curves, potentially due to the activation reaction typical of conversion-type electrodes.[25]

The galvanostatic discharge–charge profiles of $LiCuFe_2(VO_4)_3$ at a current density of 0.5 A g^{-1} are displayed in Figure 2b. During the initial discharge curve, a voltage plateau near 2.25 V corresponds to the reduction of Cu^{2+} to Cu^0 and the formation of Fe_3O_4. The plateau at 1.75 V is associated with the Li^+ insertion into the electrode material. Additionally, a distinct voltage plateau around 0.25 V is indicative of the formation of the SEI layer. In subsequent cycles, the less steep voltage profiles with plateaus at approximately 0.5 V during discharge and 1.31 V during charge are observed, which primarily correspond to the reversible electrochemical process, facilitating Li^+ storage through conversion and intercalation reactions.[26,27] The voltage plateaus are largely consistent with the peak observed in the CV measurements. The electrode exhibits initial discharge/charge capacities of 1150/850 mAh g^{-1}, yielding a coulombic efficiency of 73.9%, consistent with typical conversion-type anodes where irreversible SEI formation dominates the initial capacity loss.[28] Capacity losses in subsequent cycles may be due to the fragmentation of $LiCuFe_2(VO_4)_3$

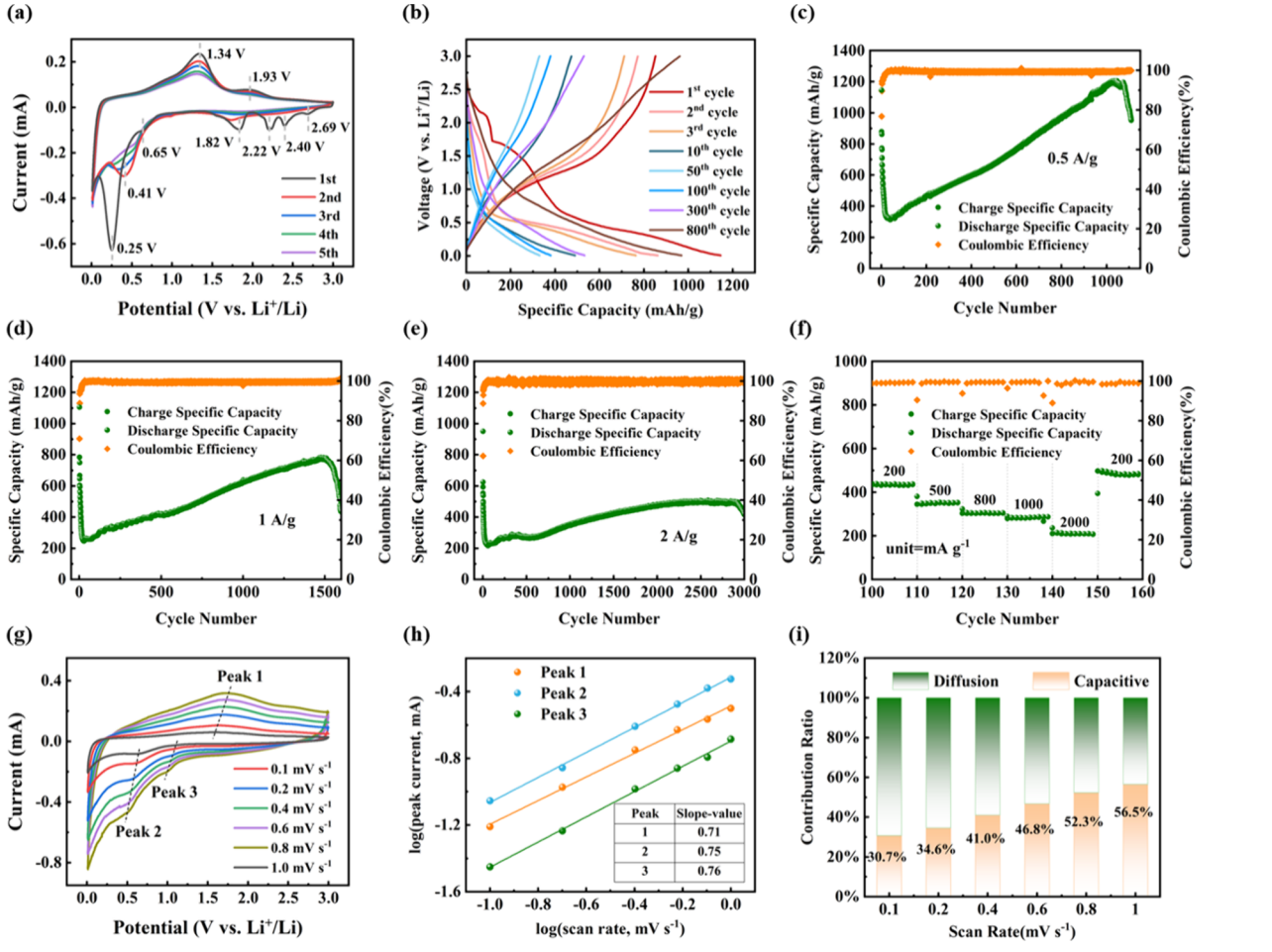


Figure 2. (a) Cyclic voltammetry curves at a scan rate of 0.1 mV s^{-1}. (b) Galvanostatic discharge–charge profiles at a current density of 0.5 A g^{-1}. Cycling performance at a current density of (c) 0.5 A g^{-1}, (d) 1 A g^{-1}, and (e) 2 A g^{-1}. (f) Rate performance of the $LiCuFe_2(VO_4)_3$ anode. (g) CV curves at different scan rates from 0.1 to 1 mV s^{-1} for the $LiCuFe_2(VO_4)_3$ anode after 100 cycles. (h) Linear relationship of (log v) and (log i) at specific peak currents. (i) Contribution ratios of capacitive and diffusion effects.

https://doi.org/10.1021/acsami.6c03927
ACS Appl. Mater. Interfaces XXXX, XXX, XXX–XXX

blocks and instability of the SEI film, characterized by continuous rupture and reconstruction.[29]

The long-term cycling performance of the $LiCuFe_2(VO_4)_3$ electrode at 0.5, 1, and 2 A g^{-1} in the range of 0.01–3.00 V vs Li^+/Li is depicted in Figure 2c–e. While an initial capacity fading is observed during the first 10 cycles, a remarkable capacity climbing phenomenon emerges subsequently. The initial capacity fading may primarily originate from the irreversible consumption of active lithium, arising from extensive SEI film formation, partly irreversible $Cu^{2+} \rightarrow Cu^0$ and $Fe^{3+} \rightarrow Fe_3O_4$ conversions with structural decomposition, together with incomplete electrochemical activation in the initial cycles.[29,30] Specifically, the electrode recovers and gradually increases in capacity, achieving 1178 and 775 mAh g^{-1} after 1000 cycles at 0.5 A g^{-1} and 1500 cycles at 1 A g^{-1}, respectively. In addition, the electrode maintains excellent performance even at high current densities, retaining a specific capacity of 497 mAh g^{-1} after 2700 cycles at a current density of 2 A g^{-1}, as depicted in Figure 2e. Rate performance, a critical indicator of battery performance, was evaluated following 100 cycles at 0.2 A g^{-1}. Figure 2f shows the battery delivering average capacities of 420, 350, 300, 290, 220, and 500 mAh g^{-1} at current densities of 0.2, 0.5, 0.8, 1, 2, and 0.2 A g^{-1}, respectively. The specific capacity decreases with increasing current density, likely due to the limiting diffusion rate of Li^+ within the material's bulk phase. Furthermore, upon reverting to 0.2 A g^{-1}, the specific capacity exceeds the initial value, demonstrating the excellent reversibility of the electrode.

To further investigate the electrochemical properties of $LiCuFe_2(VO_4)_3$, the Nyquist plots were recorded over the frequency range of 100 kHz to 0.01 Hz before and after 200 cycles, as displayed in Figure S2. Both the before and after cycling curves exhibit a semicircle and an oblique line; however, the R_{ct} of the battery before cycling shows a larger arc compared to that of the activated state after reaction. The equivalent circuit fitting reveals a significant reduction in R_{ct} from 430.90 Ω before cycling to 14.30 Ω after 200 cycles, signifying markedly enhanced electrochemical reaction kinetics,[25] corroborating the cycling and rate performance outcomes. This reduction may stem from the improved electrical conductivity due to metallic Cu precipitation and continuous material activation throughout the cycling process.[31] Detailed R_{ct} values fitted within the first 200 cycles are also presented (Figure S3), showing an aligned evolution trend with capacity increase.

In LIBs, it has been widely reported that numerous transition-metal-oxide-based electrodes exhibit extra capacity exceeding the theoretical value.[32] However, the underlying mechanism is still controversial. Figure S4 displays the SEM morphologies of the $LiCuFe_2(VO_4)_3$ electrode before and after 100 cycles at 0.5 A g^{-1}. Obviously, the electrode material after cycling is significantly reduced in size compared to its initial state, a characteristic commonly observed in conversion and alloy-type anode materials of LIBs.[33] Here, the material particle refinement caused by electrochemical reactions is referred to electrochemical activation.[30,34] It arises as fresh active materials are progressively exposed during the cycle process. The crushed active materials will increase the specific surface area of the electrode, ensuring full contact with the electrolyte.[35] This enhancement in contact reduces Li^+ diffusion path and exposes more active sites for lithium ion storage. This is also one of the reasons why the $LiCuFe_2(VO_4)_3$ anode exhibits a capacity increase phenomenon. Furthermore, the electrode after 2700 cycles at 2 A g^{-1} was also tested via SEM to evaluate the macrostructural impact of repetitive lithiation/delithiation (Figure S5). The results reveal that the electrode layer is free of apparent cracks and maintains excellent adhesion to the Cu foil current collector, demonstrating the outstanding mechanical and structural stability.

In addition to metallic Cu and the electrochemical activation process, the observed increase in capacity is also partly attributed to the polymer gel-like film within the low discharge voltage window, a result of Fe^{3+}-derived Fe_3O_4-catalyzed dynamic electrolyte translation.[12] SEM observations were conducted on the samples after 400 cycles. During the lithiation process (Figure S6), a relatively thick covering layer can be clearly observed on the particle surface of the sample. Conversely, when the sample is fully charged (Figure S7), this outer gel-like layer is nearly absent. This observation indicates that the formation and decomposition of polymer gel-like film enable the electrode material to maintain its structure and function in repeated cycles.[36] Figure S8 provides TEM images of discharged and charged states, which further confirm the reversibility of the gel-like film.

The polymer gel-like film can contribute to additional interface storage capacity through the pseudocapacitive mechanism, typically generated at voltages below 1.2 V.[37] To gain deeper insights into the evolutionary mechanism of the gel-like film and its impact on capacity enhancement, CV curves in scan rates ranging from 0.1 to 1 mV s^{-1} were conducted on batteries that were precycled for 50 cycles (Figure S9a) and 100 cycles (Figure 2g) to elucidate the dynamic behavior of the gel-like film during extended cycling and its direct correlation with the observed capacity increase. As the scan rate increases, the reduction peaks shifted to lower potentials, while the oxidation peaks shifted to higher potentials, indicative of polarization effects. The dynamics of the charge storage mechanism can be analyzed by examining the relationship between the current i and the sweep rate v, which can be described by the following equation:[35]

$$i = a \exp(b \ln v) \tag{1}$$

In eq 1, a and b are adjustable parameters. a is a constant, and the value of b ranges from 0.5 to 1.0, which can be determined by plotting the logarithm of the current (log i) vs the logarithm of the scan rate (log v) for the cathodic and anodic peaks (Figure 2h). When the fitted slope b equals 0.5, the kinetic process of Li^+ storage behavior is controlled by diffusion.[38] Conversely, b equals 1 indicates that the process is surface-controlled, which is characteristic of pseudocapacitive behavior, a Faraday process occurring on the surface of electrode materials. After 50 cycles, the electrode exhibited two characteristic redox peaks with b values of 0.66 and 0.52 (Figure S9b). Interestingly, as cycling progressed to 100 cycles, the CV curves display three distinct peaks with b values of 0.71, 0.75, and 0.76 (Figure 2h). This transition from two to three redox peaks indicates that the progressive structural evolution of the interfacial film during cycling enables the multielectron redox process to become fully resolved into a distinct feature.[39] Meanwhile, the increase in b values indicates an enhanced pseudocapacitive behavior in the charge storage process, which is controlled by a combination of diffusion and surface process. Furthermore, the contribution of diffusion and capacitive is calculated by eq 2 to quantify the improvement in the charge storage process:

$$i = k_1 v + k_2 \exp(1/2 \ln v) \tag{2}$$

https://doi.org/10.1021/acsami.6c03927
ACS Appl. Mater. Interfaces XXXX, XXX, XXX–XXX

The ratio of capacitive contributions at various sweep rates of both 50-cycled and 100-cycled electrodes is also displayed in Figure S9 and Figure 2i, respectively. For 100-cycled electrode, the capacitive contribution is 30.7% and increased to 56.5% at 1 mV s^{-1} (Figure S10). Crucially, the capacitive fractions for the 100-cycled electrode were found to be higher than those of the 50-cycled electrode at all scan rates, proving a generalized enhancement in pseudocapacitive storage. This boosted pseudocapacitive contribution indicates that the evolution of the gel-like film unlocks abundant active interfaces, rendering the electrode highly proficient in fast faradaic reactions and driving the observed capacity rise.[40]

The galvanostatic intermittent titration technique (GITT) was utilized to figure out the diffusion coefficient of Li^+ (D_{Li+}) to learn about the structural evolution of the electrochemical characteristics (Figure S11). It could be inferred that calculated D_{Li+} values ranging from 10^{-9} to 10^{-12} cm^2 s^{-1} demonstrate the rapid Li^+ diffusion during the processes of lithiation and delithiation.

Lithium Storage Mechanism of the $LiCuFe_2(VO_4)_3$ Anode

To elucidate the microstructure evolution of the $LiCuFe_2(VO_4)_3$ electrode and ascertain the formation potential of Cu^0, detailed morphological and structural characterizations were conducted at various discharge states during the first cycle with nickel foil as the current collector (Figure 3a). The SAED pattern of the electrode discharged to 2.65 V (Figure 3b) exhibits bright diffraction spots corresponding well with the multiple crystal planes of $LiCuFe_2(VO_4)_3$ (JCPDS no. 50-0212). The HRTEM image, as shown in Figure 3c, reveals distinct lattice fringes, indicating that the initial Li^+ insertion exerts minimal impact on the crystallinity of the host structure. The interplanar spacings of 0.215 and 0.328 nm are indexed to the $(1\bar{4}2)$ and (120) crystal planes of $LiCuFe_2(VO_4)_3$, respectively. The element mapping diagram (Figure 3d) further confirms the homogeneous distribution of all constituent elements. Upon discharging to 2.32 V, as shown in Figure 3e–g, the SAED image and HRTEM pattern align well with multiple crystal planes of $LiCuFe_2(VO_4)_3$. However, compared to the HRTEM image of the electrode at 2.65 V (Figure 3d), note that the apparent slight decrease in the relative brightness of the Fe signal (Figure 3h) is possibly attributed to the structural rearrangement, resulting in a nonuniform redistribution of Fe and creating regions of locally varying Fe density.[41] It is noteworthy that when discharged to 2 V, as shown in Figure 3i, scattered dark spots emerge at the edges of the material, which spatially correspond to Cu-rich regions in the element mapping (Figure 3l), indicating the nucleation of Cu^0. The SAED plot (Figure 3j) displays diffraction rings, indexed to the (111), (002), and (022) crystal planes of Cu (JCPDS no. 04-0836), moving from the center outward. The HRTEM image (Figure 3k) also shows clustered lattice fringes, matching to the (111) crystal plane of Cu^0. Collectively, these results indicate that *in situ* Cu metal nanoparticle precipitation occurs during the discharge process from 2.32 to 2 V in the first cycle, which is consistent with the analysis in CV. Although electrochemically inactive, these Cu^0 nanoparticles enhance the overall electrical conductivity of the electrode and orchestrate charge percolation networks.[42] It is worth noting that theoretical mass ratio of copper within the $LiCuFe_2(VO_4)_3$ framework is restricted to only ~12.6 wt %. The potential gravimetric penalty introduced by this portion of mass is extensively counterbalanced by the outstanding reversible capacity (1178 mAh g^{-1}) delivered by the activated multicomponent matrix. In addition, it is speculated that spin-polarized electrons may accumulate in the Cu^0 nanoparticles, forming space charge regions,[43]

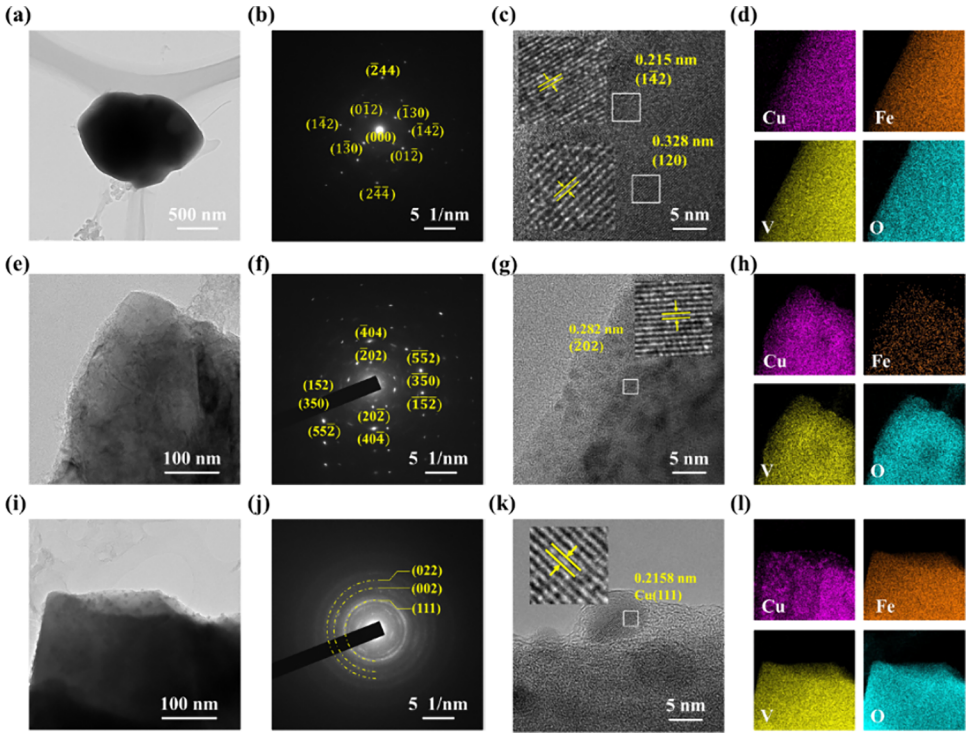


Figure 3. TEM, SAED, HRTEM, and EDS mapping images for the electrode (a–d) discharged to 2.65 V, (e–h) discharged to 2.32 V, and (i–l) discharged to 2 V at the first cycle.

https://doi.org/10.1021/acsami.6c03927
ACS Appl. Mater. Interfaces XXXX, XXX, XXX–XXX

facilitating additional Li^+ storage at grain boundaries and surfaces, which contributes additional capacity and results in the capacity elevation observed in the $LiCuFe_2(VO_4)_3$ anode.

The lithiation mechanism of $LiCuFe_2(VO_4)_3$ was investigated via *in situ* XRD, as shown in Figure 4a. During the initial stage of the first discharge cycle, diffraction peaks located at 23.9°, 27.5°, 28.1°, and 29.2° correspond to the (200), (21$\bar{1}$), (1$\bar{3}$0), and (210) crystal planes of $LiCuFe_2(VO_4)_3$, respectively. The continuous attenuation and eventual disappearance of these peaks indicate that Li^+ insertion leads to lithium saturation of the available Li^+ sites, thereby triggering phase transformation and structural decomposition of the parent compound into new species during the first discharge process. Peaks at 38.6°, 41.3°, and 43.9° originate from the beryllium (Be) window of the *in situ* XRD cell. To capture more detailed structural changes during lithiation, synchrotron radiation XRD tests were conducted on the electrodes at selected potentials under a current density of 100 mA g^{-1}, as shown in Figure 4b. At discharge potentials of 2.5 and 2.3 V, the diffraction peaks exhibit negligible alteration, suggesting that the intercalation of Li^+ at this stage has minimal effect on the $LiCuFe_2(VO_4)_3$ crystal structure. Upon further discharging to 2.0 and 1.3 V, the diffraction peaks of $LiCuFe_2(VO_4)_3$ progressively vanish, indicating that the lattice of $LiCuFe_2(VO_4)_3$ can no longer accommodate additional Li^+ and undergoes irreversible transformation reactions. New diffraction peaks emerged at 17.51° and 18.81°, corresponding to the (241) and (4$\bar{0}$4) crystal planes of Fe_3O_4 (JCPDS no. 04-18-0091). When further discharged to 0.5 V, the diffraction peaks of Fe_3O_4 disappeared, which could be due to Fe_3O_4 reacting with electrolyte, potentially catalyzing the formation of a derived interfacial layer, a reversible polymeric gel-like film.[44,45] When the second cycle reached 0.01 V, three new diffraction peaks appearing at 8.43°, 11.05°, and 11.23° belong to the (2$\bar{0}$3), (2$\bar{0}$4), and (004) crystal planes of $Li_2V_{18}O_{39}$ (JCPDS no. 04-11-4004), while the diffraction peak appearing at 11.98° corresponds to the (011) crystal plane of Li_3VO_4 (JCPDS no. 00-38-1247). During the charging process of the 2nd and 200th cycles, the (2$\bar{0}$3) and (2$\bar{0}$4) crystal planes of $Li_2V_{18}O_{39}$ as well as the (011) crystal plane of Li_3VO_4 shifted to higher angles compared to the fully discharged states, indicating the extraction of Li^+ and a decrease in interlayer spacing.[46] The (011) crystal plane of Li_3VO_4 exhibits a more pronounced shift, indicating that Li_3VO_4 stores more Li^+ than $Li_2V_{18}O_{39}$. Combined with the analysis results of TEM in Figure 3, it can be explained that during the Li^+ storage process of $LiCuFe_2(VO_4)_3$, Cu^{2+} ions are reduced and precipitate to form metallic Cu nanoparticles, which enhance the conductivity of the electrode. Simultaneously, Fe^{3+} ions undergo conversion to Fe_3O_4 during the first cycle of discharge, which may subsequently react with the electrolyte to generate a dynamically reversible polymer gel-like film,[45] providing the interface storage capacity through the pseudocapacitive mechanism. In addition, the formation of Li_3VO_4 and $Li_2V_{18}O_{39}$ contributes to lithium storage through a reversible intercalation/deintercalation mechanism, collectively accounting for the hybrid storage behavior of the $LiCuFe_2(VO_4)_3$ anode.[46]

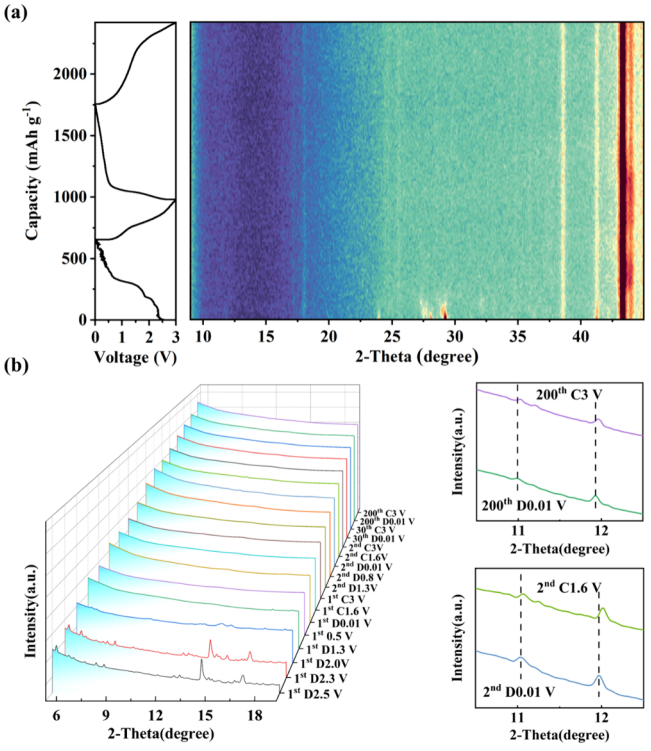


Figure 4. (a) *In situ* XRD patterns of $LiCuFe_2(VO_4)_3$ electrodes upon the first two cycles. (b) Synchrotron radiation XRD patterns of $LiCuFe_2(VO_4)_3$ electrodes at different discharge and charge states.

To verify the lithiation mechanism and Li^+ transport behavior in the $LiCuFe_2(VO_4)_3$ anode during the first discharge cycle, we performed systematic first-principles calculations. A symmetric $Li_3Cu_2Fe_4(VO_4)_6$ structure model was constructed (Figure 5a), accounting for two distinct Li^+ sites in the $LiCuFe_2(VO_4)_3$ lattice, where one site exhibits partial occupancy (50%). This model accommodates 1/3 and 2/3 excess Li^+ intercalation to simulate supersaturated lithiation conditions. The optimized lattice parameters (Table S2) reveal anisotropic volume expansion of 2.8% and 4% for $Li_4Cu_2Fe_4(VO_4)_6$ and $Li_5Cu_2Fe_4(VO_4)_6$, respectively. These lithiation processes correlated with negative Li defect formation energies (−2.463 and −2.318 eV), indicating the thermodynamic favorability of Li^+ insertion during early-stage discharge. However, the accumulated lattice strain caused by volume expansion would subsequently trigger anode phase transition, as evidenced by synchrotron radiation XRD observations of Fe_3O_4 formation at 2.0 V. To further investigate the lithiation mechanism during discharging, the Bader charge analysis of metal elements has been carried out as summarized in Table S3. The Fe charge state decreases from +1.626 to +1.171, indicating preferential Li^+ interaction at adjacent sites of FeO_6 octahedra, and Fe^{3+} acts as the redox center during lithiation. To map Li^+ migration kinetics, we evaluated different lithium diffusion pathways in the $Li_3Cu_2Fe_4(VO_4)_6$ structure (Figure S14). The lowest energy pathway (Figure 5b,c) involves Li^+ hopping along the *b* axis through the interstitial hollow sites with a transition state barrier of 0.60 eV. In this case, Li^+ form bonds to the edge-sharing O in FeO_6 octahedra with a Li−O bond length of 1.784 Å. To validate the theoretical calculation results, EIS testing was performed on aged $LiCuFe_2(VO_4)_3$-Li half-cells at 25–40 °C (Figure S15), and the charge transfer resistance (R_{ct}) was extracted through impedance fitting, as summarized in Table S4. Based on the Arrhenius equation ($\ln k = \frac{-E_a}{RT} + \ln A$),[47] the activation energy ($E_{a,ct}$) for Li^+ transport in $LiCuFe_2(VO_4)_3$ was calculated to be 0.62 eV. The remarkable consistency between experimental and computational results

https://doi.org/10.1021/acsami.6c03927
ACS Appl. Mater. Interfaces XXXX, XXX, XXX−XXX

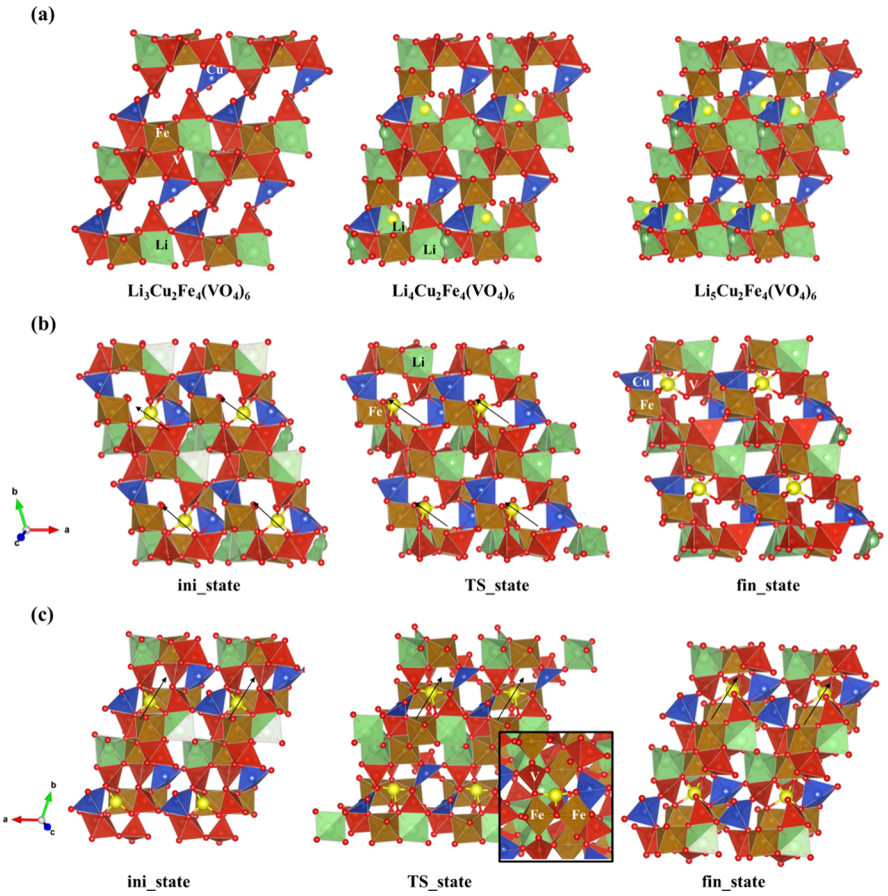


Figure 5. (a) Crystal structure diagram of $Li_{3+x}Cu_2Fe_4(VO_4)_6$ ($x = 0, 1, 2$). (b, c) The optimal migration path of Li^+ in the $Li_3Cu_2Fe_4(VO_4)_6$ structure from different angles (E_TS = 0.60 eV, *TS state imaginary frequency 179.94 cm^{-1}).

confirms the relatively low Li^+ migration barrier in $LiCuFe_2(VO_4)_3$.

Based on the comprehensive analysis above, the lithium storage mechanism of $LiCuFe_2(VO_4)_3$ is illustrated schematically. During the first discharge cycle, when the potential reaches 2.0 V, Cu^{2+} and Fe^{3+} undergo initial conversion reactions. Cu^{2+} is reduced and precipitated to form Cu nanoparticles, orchestrating charge percolation networks and accelerating the electrochemical reaction kinetics. Simultaneously, Fe^{3+} is partially reduced to Fe_3O_4, which acts as an electrochemical catalyst to facilitate the electrolyte decomposition, resulting in the formation of a polymer gel-like film. This film contributes to additional lithium storage via a pseudocapacitive mechanism, thereby promoting continuous capacity enhancement. In the second cycle, upon deep discharge to 0.01 V, the remaining structure matrix undergoes further transformation into Li_3VO_4 and $Li_2V_{18}O_{39}$, which accommodate Li^+ through a reversible insertion/extraction mechanism, complementing the hybrid storage behavior of the electrode.

■ CONCLUSIONS

In summary, a structurally engineered vanadate-based compound, $LiCuFe_2(VO_4)_3$, has been demonstrated as a low-voltage (0.4 V vs Li/Li^+), high-capacity anode material for LIBs, delivering a capacity of 1178 mAh g^{-1} after 1000 cycles at a current density of 0.5 A g^{-1} and remaining at 497 mAh g^{-1} after 2700 cycles even under a higher current density of 2 A g^{-1}. This remarkable cycling performance and continuous capacity growth are enabled by an electrochemical-induced structural optimization governed by sequential phase evolution and interface reconstruction. Through progressive lithiation, $LiCuFe_2(VO_4)_3$ undergoes a sequence of structural and interfacial transformations, ranging from conductivity enhancement to catalytic interface remodeling, that cooperatively sustain electrochemical activity and activate diverse lithium storage pathways. These coupled processes establish a hierarchical regulation paradigm that not only mitigates interfacial degradation but also reinforces long-term capacity contribution. The insights gained from this study will facilitate further exploration of polycationic metal vanadates with promising lithium storage properties, advancing the rational design of next-generation lithium storage systems with high capacity, long life, and robust rate performance.

■ EXPERIMENTAL SECTION

Preparation of $LiCuFe_2(VO_4)_3$

Powder samples of $LiCuFe_2(VO_4)_3$ were prepared by the conventional solid-phase sintering method. The stoichiometric mixtures of Li_2CO_3, CuO, Fe_2O_3, and V_2O_5 were thoroughly ground and pressed into circular plates with a thickness of about 2 mm, placed into an alumina crucible, and then calcined at 600 °C (72 h) and 640 °C (4 × 72 h) with intermediate grinding to ensure phase homogeneity.[48]

https://doi.org/10.1021/acsami.6c03927
ACS Appl. Mater. Interfaces XXXX, XXX, XXX–XXX

Characterization

The structure and *in situ* XRD of the obtained samples were characterized using powder X-ray diffractometer (XRD, Bruker D8 Advance). The Rietveld refinement (GSAS-II) was conducted to analyze the XRD patterns.[49] The morphology and microstructure of the products were characterized by scanning electron microscopy (SEM, Hitachi SU8010) and transmission electron microscopy (TEM, Tecnai G2 F20, FEI), which is equipped with an energy-dispersive spectroscopy (EDS) detector. Composition and elemental analyses were performed by an X-ray photoelectron spectrometer (XPS, ESCALAB 250Xi). Synchrotron X-ray diffraction patterns were collected at beamline BL02U2 in the Shanghai Synchrotron Radiation Facility (SSRF, Shanghai). The wavelength of the radiation source was 0.8267 Å.

Electrochemical Measurements

The electrochemical properties of the material were evaluated using coin-type cells. For the working electrode preparation, the active material ($LiCuFe_2(VO_4)_3$), acetylene black (AB, conductive agent), and polyvinylidene fluoride (PVDF) binder were mixed and ground in a mortar with a weight ratio of 7:2:1, using *N*-methyl pyrrolidone (NMP) as the solvent. The formed homogenous slurry was pasted on a copper foil and placed in a vacuum oven at 120°C for 12 h to remove the possible solvent before pressing. Standard CR2032-type coin cells were assembled in an Ar-filled glovebox (MIKROUNA), with glass microfiber filters as separator and metallic lithium as counter electrode. The 1.0 M LiPF6 electrolyte was made by mixing ethylene carbonate (EC) and dimethyl carbonate (DMC) in a 1:1 volume ratio. Cyclic voltammetry (CV) curves were carried out on a CHI660E electrochemical workstation. Electrochemical impedance spectra (EIS, Zahner) were measured over the frequency range from 100 kHz to 100 mHz. Galvanostatic discharge–charge (GDC) experiments were performed at different current densities in the 0.01–3.00 V voltage range vs Li^+/Li with a multichannel battery tester (LAND CT-2001A). All the electrochemical tests were carried out at room temperature. For postcycling SEM, TEM, XRD, and XPS analyses, the coin cells were disassembled in an Ar-filled glove box and rinsed in DMC solvent repeatedly.

■ ASSOCIATED CONTENT

Supporting Information

The Supporting Information is available free of charge at https://pubs.acs.org/doi/10.1021/acsami.6c03927.

Refined crystal structure of $LiCuFe_2(VO_4)_3$ using GSAS-2 software; (2) Nyquist plots of fresh coin cell and cell after 200 cycles; (3) Nyquist plots of electrode after 10, 30, 50 and 200 cycles; Corresponding R_{ct} values; (4) SEM images of the $LiCuFe_2(VO_4)_3$ electrodes before and after 100 cycles; (5) SEM image of the $LiCuFe_2(VO_4)_3$ electrode after 2700 cycles at 2 A g^{-1}; (6) SEM images of the $LiCuFe_2(VO_4)_3$ electrode in lithiation state after 400 cycles; (7) SEM images of the $LiCuFe_2(VO_4)_3$ electrode in delithiation state after 400 cycles; (8) TEM image of the $LiCuFe_2(VO_4)_3$ electrode after 400 cycles; (9) CV curves at different scan rates from 0.1 to 1 mV s^{-1} for $LiCuFe_2(VO_4)_3$ anode after 50 cycles; (10) capacitive contribution area of the CV curve for $LiCuFe_2(VO_4)_3$ anode after 100 cycles; (11) GITT curves and corresponding Li-ion diffusion coefficient (D_{Li+}) result; (12) high-resolution XPS spectra of Cu 2p, Fe 2p, and V 2p of $LiCuFe_2(VO_4)_3$ anode after 400 cycles; (13) high-resolution XPS spectra of C 1s, O 1s, and F 1s of $LiCuFe_2(VO_4)_3$ anode after 400 cycles; (14) the migration path of Li^+ in the $Li_3Cu_2Fe_4(VO_4)_6$ structure; (15)EIS spectra of the $LiCuFe_2(VO_4)_3$-Li half-cell at different temperatures of 25–40°C and activation energy of the charge transfer process in the $LiCuFe_2(VO_4)_3$ plate; (16) atomic parameters of $LiCuFe_2(VO_4)_3$ after refinement; (17) calculated crystallographic and defect formation energies (DFE) of $Li_{3+x}Cu_2Fe_2(VO_4)_6$ (x = 0, 1, 2) from first-principles calculations; (18) Bader charge analysis of Cu, Fe, and V in $Li_{3+x}Cu_2Fe_2(VO_4)_6$(x = 0, 1, 2); (19) fitting results of EIS spectra at different temperatures (25–40°C); and (20) electrochemical performance comparison of representative vanadate-based anodes for lithium-ion batteries (DOCX)

■ AUTHOR INFORMATION

Corresponding Author

Meicheng Li – *State Key Laboratory of Alternate Electrical Power System with Renewable Energy Sources, School of New Energy, North China Electric Power University, Beijing 102206, P. R. China;* orcid.org/0000-0002-0731-741X; Email: mcli@ncepu.edu.cn

Authors

Lihua Chu – *State Key Laboratory of Alternate Electrical Power System with Renewable Energy Sources, School of New Energy, North China Electric Power University, Beijing 102206, P. R. China; Christopher Ingold Laboratories, Department of Chemistry, University College London, 20 Gordon Street, London WC1H 0AJ, U.K.;* orcid.org/0000-0002-6664-279X

Haiyang Ye – *State Key Laboratory of Alternate Electrical Power System with Renewable Energy Sources, School of New Energy, North China Electric Power University, Beijing 102206, P. R. China*

Shiqi Liu – *Institute of Advanced Battery Materials and Devices, College of Materials Science and Engineering, Beijing University of Technology, Beijing 100124, P. R. China; State Key Laboratory of Materials Low-Carbon Recycling, Institute of Matter Science, Beijing University of Technology, Beijing 100124, P. R. China*

Junxiang Zhang – *State Key Laboratory of Alternate Electrical Power System with Renewable Energy Sources, School of New Energy, North China Electric Power University, Beijing 102206, P. R. China*

Jianan Gu – *State Key Laboratory of Alternate Electrical Power System with Renewable Energy Sources, School of New Energy, North China Electric Power University, Beijing 102206, P. R. China;* orcid.org/0000-0003-3914-5760

Mengwei Wang – *State Key Laboratory of Alternate Electrical Power System with Renewable Energy Sources, School of New Energy, North China Electric Power University, Beijing 102206, P. R. China*

Shangzhe Guo – *State Key Laboratory of Alternate Electrical Power System with Renewable Energy Sources, School of New Energy, North China Electric Power University, Beijing 102206, P. R. China*

Mengqing Li – *State Key Laboratory of Alternate Electrical Power System with Renewable Energy Sources, School of New Energy, North China Electric Power University, Beijing 102206, P. R. China*

https://doi.org/10.1021/acsami.6c03927
ACS Appl. Mater. Interfaces XXXX, XXX, XXX–XXX

Yuxin Shi – *State Key Laboratory of Alternate Electrical Power System with Renewable Energy Sources, School of New Energy, North China Electric Power University, Beijing 102206, P. R. China*

Xin Xia – *State Key Laboratory of Alternate Electrical Power System with Renewable Energy Sources, School of New Energy, North China Electric Power University, Beijing 102206, P. R. China*

Lehao Liu – *State Key Laboratory of Alternate Electrical Power System with Renewable Energy Sources, School of New Energy, North China Electric Power University, Beijing 102206, P. R. China*; orcid.org/0000-0002-7483-9197

Haifang Li – *State Key Laboratory of Alternate Electrical Power System with Renewable Energy Sources, School of New Energy, North China Electric Power University, Beijing 102206, P. R. China*

Bing Jiang – *State Key Laboratory of Alternate Electrical Power System with Renewable Energy Sources, School of New Energy, North China Electric Power University, Beijing 102206, P. R. China*

Christopher S. Blackman – *Christopher Ingold Laboratories, Department of Chemistry, University College London, 20 Gordon Street, London WC1H 0AJ, U.K.*; orcid.org/0000-0003-0700-5843

Complete contact information is available at: https://pubs.acs.org/doi/10.1021/acsami.6c03927

Author Contributions

‡L.C., H.Y., and S.L. contributed equally to this work. **Meicheng Li**: conceived the research idea, secured funding acquisition, and provided laboratory resources. **Lihua Chu**: contributed to conceptualization and funding acquisition, carried out project administration, and supervised the research progress. **Haiyang Ye**: carried out formal analysis and experimental investigation, wrote the original draft of manuscript, and carried out review and editing of manuscript. **Shiqi Liu**: developed experimental methodology, provided research resources, carried out data visualization, and contributed to review and editing of manuscript. **Junxiang Zhang**: carried out formal analysis and contributed to experimental investigation. **Jianan Gu:** supervised the research work and contributed to review and editing of manuscript. **Mengwei Wang:** carried out formal analysis, experimental investigation, and validation. **Shangzhe Guo:** carried out experimental investigation and validation. **Mengqing Li**: carried out experimental investigation and developed data processing software. **Yuxin Shi:** carried out formal analysis and experimental investigation and contributed to review and editing of manuscript. **Xin Xia:** carried out experimental investigation and data visualization. **Lehao Liu:** contributed to supervision and validation. **Haifang Li:** supervised the research work and contributed to validation. **Bing Jiang:** developed experimental methodology and contributed to supervision. **Christopher S Blackman:** contributed to research conceptualization, carried out data curation, and carried out validation.

Funding

This work is supported partially by a project of the National Natural Science Foundation of China (52402252, 62474064, 52272200, 52102203, and 52302250); Hebei Natural Science Foundation (E2022502022 and B2024502013); the project of China Three Gorges Corporation named key technologies of intelligent joint regulation and operation with grid connected friendly in power station group of wind, solar photovoltaic and energy storage (WWKY-2021-0173); and Huaneng Group Headquarters Science and Technology Project (HNKJ20-H88).

Notes

The authors declare no competing financial interest.

■ ACKNOWLEDGMENTS

We thank the Shanghai Synchrotron Radiation Facility of BL02U2 (https://cstr.cn/31124.02.SSRF.BL02U2) for the assistance on SXRD measurements.

■ REFERENCES

(1) Tan, R.; Liu, K.; Zhu, X.; Yang, S.; Zhang, Q.; Zhang, J.; Chang, Z.; Chai, P.; Wang, X.; Fontaine, O.; et al. Rational molecular design of aryl-lithium reagent enables precise chemical prelithiation of graphite anodes for achieving ideal 100% initial coulombic efficiency. *J. Am. Chem. Soc.* **2025**, *147* (25), 21865−21876.

(2) Zhang, X.; Wang, D.; Qiu, X.; Ma, Y.; Kong, D.; Müllen, K.; Li, X.; Zhi, L. Stable high-capacity and high-rate silicon-based lithium battery anodes upon two-dimensional covalent encapsulation. *Nat. Commun.* **2020**, *11* (1), 3826.

(3) Thapa, A.; Gao, H. High areal loading silicon nanoparticle-based lithium-ion batteries. *ACS Appl. Mater. Interfaces* **2025**, *17* (6), 9219−9230.

(4) Huang, J. Y.; Zhong, L.; Wang, C. M.; Sullivan, J. P.; Xu, W.; Zhang, L. Q.; Mao, S. X.; Hudak, N. S.; Liu, X. H.; Subramanian, A.; et al. In situ observation of the electrochemical lithiation of a single SnO_2 nanowire electrode. *Science* **2010**, *330* (6010), 1515−1520.

(5) Ren, S.; Dong, C.; Ma, L. 3D assembly of SnO_2 onto the titanate free-standing film covered with carbon shell for enhanced lithium storage performance. *Appl. Surf. Sci.* **2026**, *718*, No. 164958.

(6) Liu, S.; Jia, K.; Yang, J.; He, S.; Liu, Z.; Wang, X.; Qiu, J. Encapsulating flower-like MoS_2 nanosheets into interlayer of nitrogen-doped graphene for high-performance lithium-ion storage. *Chem. Eng. J.* **2023**, *475*, No. 146181.

(7) Yang, G.; Cui, H.; Yang, G.; Wang, C. Self-assembly of $Co_3V_2O_8$ multilayered nanosheets: controllable synthesis, excellent Li-storage properties, and investigation of electrochemical mechanism. *ACS Nano* **2014**, *8* (5), 4474−4487.

(8) Li, P.; Zhu, C.; Chen, X.; He, M.; Sun, B.; Pei, C.; Zhang, D.; Ni, S. Self-adaptive built-in electric fields drive high-rate lithium-ion storage in $C@Li_3VO_4$ heterostructures. *Adv. Funct. Mater.* **2025**, *35* (43), No. 2503584.

(9) Hsiao, Y.-S.; Huang, J.-H.; Weng, L.-Y.; Cheng, T.-H.; Chiang, H.-H.; Lu, C.-Z.; Weng, H.-C.; Thomsen, L.; Cowie, B.; Kong Pang, W.; et al. Advancing Li_3VO_4 as a high-performance anode material for use in lithium-ion batteries and lithium-ion capacitors. *Chem. Eng. J.* **2024**, *489*, No. 150973.

(10) Li, G.; Ouyang, T.; Xiong, T.; Jiang, Z.; Adekoya, D.; Wu, Y.; Huang, Y.; Balogun, M.-S. All-carbon-frameworks enabled thick electrode with exceptional high-areal-capacity for Li-ion storage. *Carbon* **2021**, *174*, 1−9.

(11) Cui, R.; Lin, J.; Cao, X.; Hao, P.; Xie, X.; Zhou, S.; Wang, Y.; Liang, S.; Pan, A. In situ formation of porous $LiCuVO_4/LiVO_3$/C nanotubes as a high-capacity anode material for lithium ion batteries. *Inorg. Chem. Front.* **2020**, *7* (2), 340−346.

(12) Zeng, Z.; Zhao, H.; Lv, P.; Zhang, Z.; Wang, J.; Xia, Q. Electrochemical properties of iron oxides/carbon nanotubes as anode material for lithium ion batteries. *J. Power Sources* **2015**, *274*, 1091−1099.

(13) Koshelev, A. V.; Zakharov, K. V.; Pyatakov, A. P.; Shvanskaya, L. V.; Shakin, A. A.; Volkova, O. S.; Chareev, D. A.; Kamusella, S.; Klauss, H.-H.; Molla, K.; et al. Spin-order-induced ferroelectricity and

magnetoelectric effect in $LiCuFe_2(VO_4)_3$. *Phys. Rev. Appl.* **2018**, *10* (3), No. 034008.
(14) Drokina, T. V.; Petrakovskii, G. A.; Bayukov, O. A.; Vorotynov, A. M.; Velikanov, D. A.; Molokeev, M. S. Synthesis and Structural, Magnetic, and Resonance Properties of the $LiCuFe_2(VO_4)_3$ Compound. *Phys. Solid State* **2016**, *58* (10), 1981−1988.
(15) Sekhar, S. C.; Ramulu, B.; Narsimulu, D.; Arbaz, S. J.; Yu, J. S. Metal−organic framework-derived $Co_3V_2O_8$@CuV_2O_6 hybrid architecture as a multifunctional binder-free electrode for Li-ion batteries and hybrid supercapacitors. *Small* **2020**, *16* (48), No. 2003983.
(16) Xiong, F.; Lv, F.; Tang, C.; Zhang, P.; Tan, S.; An, Q.; Guo, S.; Mai, L. In situ construction of amorphous hierarchical iron oxyhydroxide nanotubes via selective dissolution-regrowth strategy for enhanced lithium storage. *Sci. China Mater.* **2020**, *63* (10), 1993−2001.
(17) Dong, L.-W.; Xu, R.-G.; Wang, P.-P.; Sun, S.-C.; Li, Y.; Zhen, L.; Xu, C.-Y. Layered potassium vanadate $K_2V_6O_{16}$ nanowires: a stable and high capacity cathode material for calcium-ion batteries. *J. Power Sources* **2020**, *479*, No. 228793.
(18) Shao, M.; Hou, S.; Li, X.; Yang, H.; Huang, Y.; Liu, Z.-Q. Dual-channel charge manipulation for enhancing charge separation and transfer kinetics in $BiVO_4$ photoanodes. *ACS Catal.* **2026**, *16* (4), 4017−4027.
(19) Xiang, J. Y.; Tu, J. P.; Zhang, L.; Zhou, Y.; Wang, X. L.; Shi, S. J. Self-assembled synthesis of hierarchical nanostructured CuO with various morphologies and their application as anodes for lithium ion batteries. *J. Power Sources* **2010**, *195* (1), 313−319.
(20) Wang, J.; Guo, X.; Du, X.; Liang, J.; Wu, J.; Zhao, G.; Li, X.; Gui, S.; Zheng, F.; Zhao, J.; et al. Revealing the complex lithiation pathways and kinetics of core-shell NiO@CuO electrode. *Energy Storage Mater.* **2022**, *51*, 11−18.
(21) Gao, M.; Dong, Q.; Yao, M.; Wang, X.; Li, J.; Zhang, W.; Huang, H.; Guo, H.; Sun, Z.; Chen, Q.; et al. Dual-gradient engineering of urchin-like silver@copper oxide heterostructures for highly stable lithium metal anodes. *Adv. Funct. Mater.* **2024**, *34* (28), No. 2401442.
(22) Ni, S.; Ma, J.; Zhang, J.; Yang, X.; Zhang, L. Electrochemical performance of cobalt vanadium oxide/natural graphite as anode for lithium ion batteries. *J. Power Sources* **2015**, *282*, 65−69.
(23) Kakarla, A. K.; Narsimulu, D.; Patnam, H. R.; Shanthappa, R.; Yu, J. S. Structural and electrochemical properties of mesoporous $FeVO_4$ as a negative electrode for lithium-ion battery. *Int. J. Energy Res.* **2022**, *46* (10), 13590−13601.
(24) Liu, X.; Cao, Y.; Zheng, H.; Chen, X.; Feng, C. Synthesis and modification of $FeVO_4$ as novel anode for lithium-ion batteries. *Appl. Surf. Sci.* **2017**, *394*, 183−189.
(25) Zhu, C.; Liu, Z.; Wang, J.; Pu, J.; Wu, W.; Zhou, Q.; Zhang, H. Novel Co_2VO_4 anodes using ultralight 3D metallic current collector and carbon sandwiched structures for high-performance Li-ion batteries. *Small* **2017**, *13* (34), No. 1701260.
(26) Chen, P.; Zhou, W.; Xiao, Z.; Li, S.; Chen, H.; Wang, Y.; Wang, Z.; Xi, W.; Xia, X.; Xie, S. In situ anchoring MnO nanoparticles on self-supported 3D interconnected graphene scroll framework: a fast kinetics boosted ultrahigh-rate anode for Li-ion capacitor. *Energy Storage Mater.* **2020**, *33*, 298−308.
(27) Khanam, Z.; Xiong, T.; Yang, F.; Su, H.; Luo, L.; Li, J.; Koroma, M.; Zhou, B.; Mushtaq, M.; Huang, Y.; et al. Endogenous interfacial Mo-C/N-Mo-S bonding regulates the active Mo sites for maximized li^+ storage areal capacity. *Small* **2024**, *20* (31), No. 2311773.
(28) Liu, H.; Chang, J. $CeVO_4$ yolk-shell microspheres constructed by nanosheets with enhanced lithium storage performances. *J. Alloys Compd.* **2020**, *849*, No. 156682.
(29) Wu, H.; Jia, H.; Wang, C.; Zhang, J.-G.; Xu, W. Recent progress in understanding solid electrolyte interphase on lithium metal anodes. *Adv. Energy Mater.* **2021**, *11* (5), No. 2003092.
(30) Ni, S.; Liu, J.; Chao, D.; Mai, L. Vanadate-based materials for Li-ion batteries: the search for anodes for practical applications. *Adv. Energy Mater.* **2019**, *9* (14), No. 1803324.
(31) Ghani, F.; Raza, A.; Kyung, D.; Kim, H.-S.; Lim, J.; Nah, I. W. Optimization of synthesis conditions of high−tap density $FeVO_4$ hollow microspheres via spray pyrolysis for lithium−ion batteries. *Appl. Surf. Sci.* **2019**, *497*, No. 143718.
(32) Garapati, M. S.; Sundara, R. Retracting interphasial stored Li^+ ions by transition metal/metal carbide nanoparticles for enhanced Li^+ ion storage capacity. *J. Colloid Interface Sci.* **2021**, *582*, 1213−1222.
(33) Li, M.; Yang, X.; Wang, C.; Chen, N.; Hu, F.; Bie, X.; Wei, Y.; Du, F.; Chen, G. Electrochemical properties and lithium-ion storage mechanism of $LiCuVO_4$ as an intercalation anode material for lithium-ion batteries. *J. Mater. Chem. A* **2015**, *3* (2), 586−592.
(34) Cui, M.; Liu, M.; Li, X.; Shi, W.; Yu, Y.; Li, J.; Liu, Y.; Zhang, F.; Wang, W.; Li, X.; et al. Order-disorder structural engineering of vanadium oxide anode: balancing ionic and electronic dynamic for fast-charging aqueous Li-ion battery. *Energy Storage Mater.* **2024**, *70*, No. 103453.
(35) Li, Z.; Huai, L.; Li, S.; Ma, M.; Luo, K.; Zhao, Y.; Wang, D.; Sun, X.; Peng, Z. Insight into bulk charge transfer of lithium metal anodes by synergism of nickel seeding and LiF-Li_3N-Li_2S co-doped interphase. *Energy Storage Mater.* **2021**, *37*, 491−500.
(36) Zhai, F.; Zhu, X.; Zhang, W.; Cao, G.; Zhang, H.; Xing, Y.; Xiang, Y.; Zhang, S. Insight of the evolution of structure and energy storage mechanism of $(FeCoNiCrMn)_3O_4$ spinel high entropy oxide in life-cycle span as lithium-ion battery anode. *J. Power Sources* **2024**, *603*, No. 234418.
(37) Luo, J.; Liu, J.; Zeng, Z.; Ng, C. F.; Ma, L.; Zhang, H.; Lin, J.; Shen, Z.; Fan, H. J. Three-dimensional graphene foam supported Fe_3O_4 lithium battery anodes with long cycle life and high rate capability. *Nano Lett.* **2013**, *13* (12), 6136−6143.
(38) Li, J.; Ouyang, T.; Liu, L.; Jiang, S.; Huang, Y.; Balogun, M.-S. A high Li-ion diffusion kinetics in multidimensional and compact-structured electrodes via vacuum filtration casting. *J. Energy Chem.* **2024**, *93*, 368−376.
(39) Sun, W.; Yi, X.; Huang, S.; Du, J.; Chen, Y.; Sun, A. Structural engineering of manganese-doped copper vanadate for enhanced pseudocapacitive ammonium-ion storage. *J. Energy Storage* **2026**, *143*, No. 119729.
(40) Choi, C.; Ashby, D. S.; Butts, D. M.; DeBlock, R. H.; Wei, Q.; Lau, J.; Dunn, B. Achieving high energy density and high power density with pseudocapacitive materials. *Nat. Rev. Mater.* **2019**, *5* (1), 5−19.
(41) Wang, F.; Li, T.; Fang, Y.; Wang, Z.; Zhu, J. Heterogeneous structured Mn_2O_3/Fe_2O_3 composite as anode material for high performance lithium ion batteries. *J. Alloys Compd.* **2021**, *857*, No. 157531.
(42) Zhang, S.; Peng, S.; Hu, R.; Ramakrishna, S. Copper vanadates/polyaniline composites as anode materials for lithium-ion batteries. *RSC Adv.* **2015**, *5* (27), 20692−20698.
(43) Li, Q.; Li, H.; Xia, Q.; Hu, Z.; Zhu, Y.; Yan, S.; Ge, C.; Zhang, Q.; Wang, X.; Shang, X.; et al. Extra storage capacity in transition metal oxide lithium-ion batteries revealed by in situ magnetometry. *Nat. Mater.* **2021**, *20* (1), 76−83.
(44) Choi, Y. S.; Choi, W.; Yoon, W.-S.; Kim, J. M. Unveiling the genesis and effectiveness of negative fading in nanostructured iron oxide anode materials for lithium-ion batteries. *ACS Nano* **2022**, *16* (1), 631−642.
(45) Ren, H.; Li, H.; Barry, P.; Wang, Z.; Campos, A. R.; Takeuchi, E. S.; Marschilok, A. C.; Yan, S.; Takeuchi, K. J.; Reichmanis, E. Recent advances in the application of magnetite (Fe_3O_4) in lithium-ion batteries: synthesis, electrochemical performance, and characterization techniques. *Chem. Mater.* **2024**, *36* (19), 9299−9319.
(46) Li, H.; Liu, X.; Zhai, T.; Li, D.; Zhou, H. Li_3VO_4: a promising insertion anode material for lithium-ion batteries. *Adv. Energy Mater.* **2013**, *3* (4), 428−432.
(47) Sun, L.; Li, M.; Gu, J.; Li, Y.; Liu, J.; Li, Y.; Li, M. High-zeta-potential accelerates interface charge transfer in lithium anodes via MXene-graphdiyne heterojunction layers. *Chem. Eng. J.* **2023**, *469*, No. 144014.
(48) Kamoun, S.; Hlel, F.; Gargouri, M. Electrical properties and conductivity mechanism of $LiCuFe_2(VO_4)_3$. *Ionics* **2014**, *20* (8), 1103−1110.
(49) Toby, B. H.; Von Dreele, R. B. GSAS-II : the genesis of a modern open-source all purpose crystallography software package. *J. Appl. Crystallogr.* **2013**, *46* (2), 544−549.

https://doi.org/10.1021/acsami.6c03927
ACS Appl. Mater. Interfaces XXXX, XXX, XXX−XXX